The Relative Importance of Stratiform and Convective Rainfall in Rapidly Intensifying Tropical Cyclones

CHENG TAO, HAIYAN JIANG, AND JONATHAN ZAWISLAK

Department of Earth and Environment, Florida International University, Miami, Florida

(Manuscript received 15 August 2016, in final form 15 December 2016)

ABSTRACT

Using 16-yr Tropical Rainfall Measuring Mission (TRMM) Precipitation Radar (PR) observations, rainfall properties in the inner-core region of tropical cyclones (TCs) and the relative importance of stratiform and convective precipitation are examined with respect to the evolution of rapid intensification (RI) events. The onset of RI follows a significant increase in the occurrence and azimuthal coverage of stratiform rainfall in all shear-relative quadrants, especially upshear left. The importance of the increased stratiform occurrence in RI storms is further confirmed by the comparison of two groups of slowly intensifying (SI) storms with one group that underwent RI and the other that did not. Statistically, SI storms that do not undergo RI during their life cycle have a much lower percent occurrence of stratiform rain within the inner core. The relatively greater areal coverage of stratiform rain in RI cases appears to be related to the moistening/humidification of the inner core, particularly in the upshear quadrants. In contrast to rainfall frequency, rainfall intensity and total volumetric rain do not increase much until several hours after RI onset, which is more likely a response or positive feedback rather than the trigger of RI. Despite a low frequency of occurrence, the overall contribution to total volumetric rain by convective precipitation is comparable to that of stratiform rain, owing to its intense rain rate.

1. Introduction

Although the intensity guidance of tropical cyclones (TCs) has achieved statistically significant improvements in the past few decades, forecasting the rapid intensification (RI) of TCs still remains problematic (DeMaria et al. 2014). It is now well known that RI most commonly occurs under favorable environmental conditions (Kaplan and DeMaria 2003; Kaplan et al. 2010, 2015; Wang and Wu 2004), including warm sea surface temperatures (SSTs) and a deep warm oceanic mixed layer, low vertical wind shear, high lower-tropospheric relative humidity, conditional instability, etc. However, it is generally accepted that favorable environmental conditions alone are not sufficient for an accurate forecast of RI (Hendricks et al. 2010). Besides the environmental scale, processes operating on vortex and convective scale are also important in determining the likelihood of RI.

Rainfall and convection within the inner-core region of TCs have been linked with RI in several satellite-based observational studies, such as Jiang (2012), Jiang and Ramirez (2013), Zagrodnik and Jiang (2014, hereafter ZJ14), Alvey et al. (2015, hereafter AZZ15), and Tao and Jiang (2015). RI was first defined by Kaplan and DeMaria (2003) as a 24-h period with intensity increase $\geq$30 kt (1 kt = 0.5144 m s^{-1}). Each 24-h period was treated as a separate *case*. All the satellite-based statistical studies mentioned above took this approach to define RI. Some studies (Jiang and Ramirez 2013; ZJ14; AZZ15; Tao and Jiang 2015) also defined other intensity change categories (i.e., slowly intensifying, neutral, and weakening) using the same approach, similar to Hendricks et al. (2010). Statistical studies benefit greatly from this case-based approach for better understanding the properties of storms that undergo RI by comparing RI cases with other intensity change categories. It also helps advance RI prediction because it uses the 24-h future intensity increase to define RI cases. However, these satellite-based studies defined RI cases by only looking at the storm intensities at the satellite overpass time and 24-h future. The main drawback of this approach is that it neglects the storm evolution information. As pointed out by Kieper and Jiang (2012), as each TC evolves, RI usually happens as an *event,* which can last as long as 48–60 h.

Corresponding author e-mail: Dr. Haiyan Jiang, haiyan.jiang@fiu.edu

DOI: 10.1175/MWR-D-16-0316.1

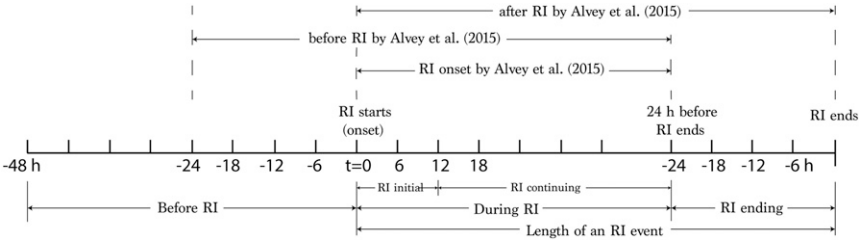

FIG. 1. Schematic of before RI, RI initial, RI continuing, and RI ending periods within a typical RI event defined using the best track data. Also placed on the timeline in the RI event are the corresponding periods of before RI, RI onset, and after RI defined by AZZ15 mentioned in section 2a. Please see text for details.

The studies using the RI case-based-only definition have a problem of not being able to place the individual case within the context of the entire RI event. Although the case-based approach causes no problem when only comparing RI cases with slowly intensifying, neutral, or weakening cases, it does cause some challenges when studying the evolution of an RI event/storm. The approach does not distinguish between stages of an RI event, including before RI onset, at or around RI onset, during the middle (or continuing stage) of an RI event, and the ending period of an RI event.

ZJ14 was the first satellite-based statistical study that embraced the concept of RI as an event. By looking at the time series of each storm's best track intensity, they defined the onset of RI as the starting time of each RI *event* instead of that of each 24-h RI *period/case*. Then they separated all RI cases into two subcategories based on their stages relative to the onset of the RI events: overpasses that occurred within 12 h of an RI onset, categorized as the *RI initial* stage, and overpasses that occurred during a period in which the storm had a previous 24-h RI case beginning at 12, 18, or 24 h prior to the overpass, categorized as the *RI continuing* stage. The RI event in both subcategories continued for at least 24 h following the overpass as well. Tao and Jiang (2015) followed ZJ14's method to define the RI initial and continuing subcategories. Therefore, both studies were able to demonstrate the evolution of precipitation and convection distributions during RI events from the beginning to the middle of RI. In this study, we will follow the same *event-based* approach, but go further by extending the analysis into before RI onset and during the ending period of RI events [defined as less than 24 h before the ending time of an RI event; cf. Fig. 13 of Tao and Jiang (2015), or Fig. 1 here]. Our goal is to complement these studies by using the same RI event-based definition to further examine the evolution of precipitation distributions during the entire life cycle of RI events.

In addition to a composite framework, some recent observational studies have also taken a case study approach to examine the convective evolution during RI; for example, for Hurricane Earl (2010) (Stevenson et al. 2014; Susca-Lopata et al. 2015; Rogers et al. 2015) and Hurricane Edouard (2014) (Rogers et al. 2016; Zawislak et al. 2016). While these and numerous other studies (e.g., Kelley et al. 2004; Hendricks et al. 2004; Reasor et al. 2009; Guimond et al. 2010; Rogers et al. 2013, 2015; Harnos and Nesbitt 2016) emphasized the role of extremely deep convection in the intensification of TCs, few studies have also examined the relative importance of stratiform precipitation in RI. Using the Tropical Rainfall Measuring Mission (TRMM) Precipitation Radar (PR) data, Fritz et al. (2016) studied the evolution of stratiform precipitation and three types of convective precipitation (i.e., shallow convection, mid-level convection, and deep convection) during TC formation in the Atlantic. They found that stratiform precipitation contributed ~80% of the increased precipitation from 3 days before genesis to 1 day after genesis, and therefore concluded that the formation of TCs could be a combined result of both convective and stratiform precipitation processes. Although they only examined tropical cyclogenesis, the results of Fritz et al. (2016) motivated the need to examine the role of stratiform rain in TC intensification.

Progress toward an improved RI prediction suffers from a continued relative lack of understanding on the contributions of convective and precipitation processes to TC intensification and their interactions with, and feedback to, the structure and evolution of the thermodynamic and kinematic fields of TCs. A long-standing debate in the field has been on symmetric and asymmetric processes and their roles in TC intensification. It has been long known that the cooperative interaction between the symmetric primary and secondary circulation patterns is important in TC intensification (Ooyama 1969; Smith 1981; Shapiro and Willoughby 1982). The azimuthally averaged latent heating release is deemed much more important for the vortex intensification than asymmetric heating (Nolan and Grasso 2003; Nolan et al. 2007).

Asymmetric mechanisms usually involve smaller-scale processes, which could interact with the vortex through a process of axisymmetrization (Houze 2010). One example of asymmetric processes involves asymmetric deep convection in the inner-core region.

This study differs from previous observational studies in that it focuses on the relative importance of stratiform versus convective precipitation types during the symmetric process of RI. This will help advance our understanding in general TC intensification and RI prediction. More importantly, as mentioned above, this work will analyze RI by applying the concept of RI events. Observations from the TRMM PR are classified into several RI event-based categories (i.e., before RI onset, RI initial, RI continuing, and in the ending period of RI) by their time relative to the onset/end of each RI event. In this study, precipitation in the inner-core region of TCs will be separated into stratiform and convective based on the TRMM 2A23 algorithm, and their contribution to the rainfall frequency, mean near-surface rain rate, and total volumetric rain will be statistically quantified within the time evolution of RI events. By comparing the rainfall properties of all types of precipitation, and stratiform and convective only among various RI event-based categories, the role of stratiform and convective precipitation in different stages of RI events will be better understood. Section 2 describes the data and methods applied in this study. The time evolution and shear-relative distributions of convective and stratiform precipitation at different stages of RI events are discussed in section 3. Section 4 compares the rainfall properties between storms that undergo RI from those that never rapidly intensify during their life cycle. The discussion and conclusions are presented in section 5.

2. Data and methodology

a. RI event-based dataset

The best track data from the National Hurricane Center (NHC) and Joint Typhoon Warning Center (JTWC) are used to determine RI events from a total of 1518 TCs between 1998 and 2013. An RI event is defined as multiple, continuous, and overlapping 24-h periods where the maximum sustained winds of each period increased by at least 30 kt, as illustrated in Fig. 1. Please also see Fig. 2 of Kieper and Jiang (2012) for an illustration of Hurricane Wilma (2005)'s RI event. Here, each 24-h period within an RI event refers to one RI case in Kaplan and DeMaria (2003). The *onset* of an RI event (labeled as "RI starts" in Fig. 1) is defined as the starting time of the first 24-h RI case within the RI event. The ending time of an RI event (labeled as "RI ends" in Fig. 1) is the ending time of the last 24-h RI case within the RI event. As defined by ZJ14, the RI initial period is within 12 h after RI onset, while the RI continuing period refers to the period between 12 h after RI onset and 24 h before RI ends. In the following text, we collectively call "RI initial" and "RI continuing" periods as "during RI." The RI ending period refers to the 24-h period between 24 h before RI ends and the ending time of this RI event. Unlike RI initial and RI continuing categories, which require at least 24 h before an RI event ends, the RI ending category has no predictive power and may correspond to the slowly intensifying (SI), neutral (N), or weakening category as defined by Tao and Jiang (2015).

AZZ15 composited satellite overpasses 0–24 h before and after RI onset and identified the starting time of each 24-h RI period/case as the onset of RI ("0" h). RI in their study is defined based on individual 24-h RI periods/cases, and thus has no "during RI" category because it treats each 24 h case as a separate event. Their definition will be identical to our RI event-based definition only when the real RI event lasts for only 24 h. As indicated in Fig. 1, their "RI onset" could be anywhere *during RI* in our definition. Their "before RI" category could be from overpasses falling into either our *before RI* or *during RI* categories. Their "after RI" category likely contains a mixture of overpasses from either *during RI* or *RI ending* period, as defined in this study. Therefore, their definitions for the before RI and after RI categories are fundamentally different from those defined using an RI event concept. So one needs to be very careful when interpreting their results because their RI onset, or even cases for "before" RI onset, could be already far into the middle of an RI event.

Out of 1518 global TCs between 1998 and 2013, 552 TCs underwent RI. Here, 700 RI events are identified due to some storms having more than one RI event during their lifetime. The length of an RI event is defined as the duration between when RI starts and RI ends. The minimum length is 24 h. Within the TC samples used in this study, the maximum length of an RI event is 78 h and the mean length is about 38 h. Table 1 lists the number and percentage of RI events in each length category from 24 to 78 h. We can see that only 24.4% of RI events last only 24 h. The majority of the RI events last more than 24 h. This fact justifies the need of defining RI using the RI event-based definition in order to better illustrate the evolution of precipitation during the life cycle of RI storms.

b. Selection of TRMM PR overpasses

The dataset for this study is derived from the TRMM Tropical Cyclone Precipitation Feature (TCPF)

TABLE 1. Number and percentage of RI events in each length category.

	Event length (h)										
	24	30	36	42	48	54	60	66	72	78	All
No. of RI events	171	129	93	125	78	49	25	21	6	3	700
Precentage of RI events	24.4	18.4	13.3	17.9	11.1	7.0	3.6	3.0	0.9	0.4	100.0

database (Jiang et al. 2011), which includes the overpasses of all global TCs viewed by the TRMM satellite. The storm center is interpolated from the best track data for TRMM observations between 1998 and 2013, and is manually adjusted to better align with the representation of PR and TMI 37-GHz channel, following ZJ14. Two additional datasets that supplement the TRMM database are included to characterize the large-scale environmental conditions in which each TC is embedded. The SST is obtained from the Reynolds daily SST grid point (at a spatial grid resolution of 0.25°) nearest to the storm center (Reynolds et al. 2007). The total precipitable water (TPW) and wind field data are derived from the 0.75°-resolution European Centre for Medium-Range Weather Forecasts (ECMWF) interim reanalysis dataset (Simmons et al. 2007). The TPW of each case refers to the azimuthal average of the innermost 250 km around the TC center. The vertical wind shear is the difference between the averaged wind vectors at the 200 and 850 hPa. Following Hence and Houze (2011), the wind vectors are averaged within a ring of 500–750 km from the TC center to eliminate the influence of the storm's circulation as much as possible.

Several criteria have been applied to the selection of TRMM overpasses in order to subset those events that are of most interest to this study: 1) the interpolated storm center must be over water at the current observational time, as well as 24 h in the future (i.e., cases with land interaction are not considered); 2) a valid PR overpass must capture the storm center (i.e., at least 50% of the storm is within the PR swath); and 3) storms that are tropical depressions (maximum sustained wind less than 34 kt) and major hurricanes (maximum sustained wind greater than 95 kt) are excluded, following ZJ14. Generally, tropical depressions rarely rapidly intensify and the intensity changes of major hurricanes are most commonly associated with eyewall replacement cycles (Willoughby et al. 1982), which is beyond the topic of this study.

The effects of the environmental conditions also need to be considered before completing the final dataset. Figure 2 shows the composite evolution of SST, 200–850-hPa environmental wind shear magnitude, TPW, and storm motion throughout the RI events. Derived from a larger dataset, which includes all well observed TRMM TMI overpasses (which are able to capture the innermost 200-km area due to a larger swath than PR), Fig. 2 indicates that environmental conditions alone cannot predict RI onset, consistent with the conclusions of Hendricks et al. (2010). Although not shown, the chance of RI does decrease for more unfavorable environments, such as low SST, high vertical wind shear, and small TPW (Kaplan and DeMaria 2003; Wang and Wu 2004; Kaplan et al. 2010; Kaplan et al. 2015). Based on the extreme values (maximum or minimum, depending on the parameter) of the selected parameters during RI period (i.e., from RI onset to 24 h before RI ends), four cutoff criteria including SST $\geq$ 25.8°C, shear $\leq$ 14.1 m s^{-1}, TPW $\geq$ 48.7 mm, and storm motion $\leq$ 10.8 m s^{-1}, have been determined to eliminate those overpasses associated with more unfavorable environmental conditions for RI. Therefore, by excluding storms in unfavorable environments our results will emphasize the role of different types of precipitation before and throughout the RI events given only semi-favorable to favorable environmental conditions.

Based on the TRMM observational time and the start/end time of RI events, the selected PR overpasses are classified into 14 categories as listed in Table 2. Also displayed in Table 2 is the number of selected PR overpasses in various future 24-h intensity change categories, including RI, slowly intensifying (SI, $10 \leq \Delta V_{\max} + 24 < 30$ kt), neutral (N, $-10 < \Delta V_{\max} + 24 < 10$ kt), and weakening (W, $\Delta V_{\max} + 24 \leq -10$ kt). Please refer to Jiang and Ramirez (2013) for further details of definitions of different intensity change categories. The dataset of this study mainly consists of overpasses associated with SI (51.9%) and RI (30.4%) storms. It should be noted that the number of selected PR overpasses are nearly uniformly distributed across each day (not shown), and thus the results shown in this study are not biased by the diurnal variation of TC rainfall.

c. *Storm properties and environmental conditions*

Table 3 shows the mean values of the maximum sustained winds, SST, vertical wind shear magnitude, TPW, storm motion, and the azimuthal difference between the directions of shear and motion vector for the final dataset. To obtain larger sample sizes, the 6-hourly time periods originally differentiated within the RI events

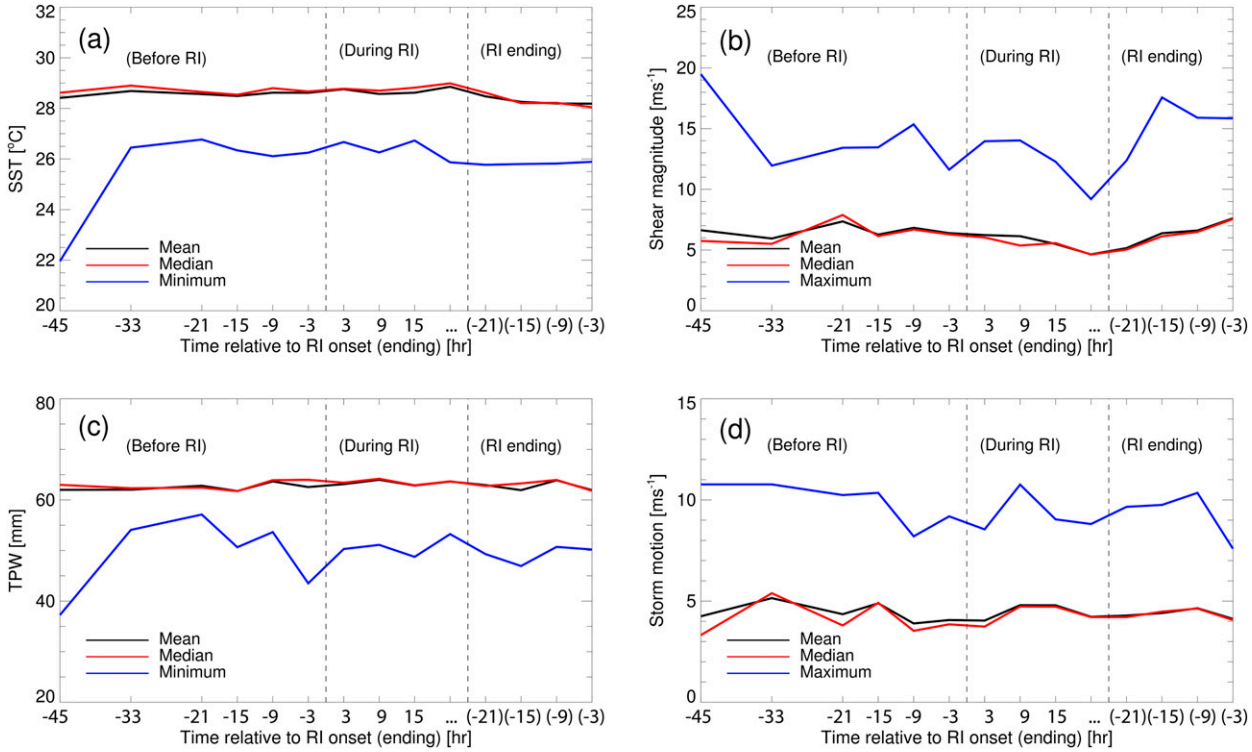

FIG. 2. Evolution of mean, median, and maximum/minimum values of environmental conditions: (a) SST, (b) shear magnitude, (c) TPW, and (d) storm motion over time. Time is defined as in Fig. 1. Dashed lines from left to right represent RI onset and 24 h before RI ends.

(Table 2) are grouped together (Table 3); the before RI period is separated into 0–12, 12–24, and 24–48 h before RI, while the during RI period is separated into RI initial and RI continuing (ZJ14), while the "RI ending" period is separated into 12–24 and 0–12 h prior to the end of RI. Statistical significance levels derived from the Student's *t* test indicate that storms that have been undergoing RI for over 12 h (i.e., RI continuing) present significantly higher intensity and lower vertical wind shear than those within 12 h of the RI onset (i.e., RI initial), while the intensity significantly increases from 12–24 to 0–12 h before RI ends. In contrast, environmental conditions are not significantly different during the period prior to, and during the initial stages after, RI onset.

3. Evolution of rainfall in rapidly intensifying TCs

a. Time evolution

Before considering the relative importance of stratiform and convective rainfall in rapidly intensifying TCs, we first examine the time evolution of azimuthally averaged rainfall properties before and throughout the RI events. The Hovmöller diagrams shown in Fig. 3 are generated by grouping the PR pixels from 14 RI event-based categories (Table 2) into 10-km annuli bins extending radially outward from the center. Using near-surface rain rates derived from version 7 (V7) of the PR 2A25 algorithm ($5 \times 5\,km^2$; $4.3 \times 4.3\,km^2$ before the orbital boost; Iguchi et al. 2009), the rainfall frequency is defined as the percent occurrence of near-surface rain rate $>0\,mm\,h^{-1}$. The total volumetric rain is the sum of the product of near-surface rain rate and area of each PR pixel normalized by the number of pixels, following Tao and Jiang (2015).

Generally, the evolution of rainfall properties changes little with time beyond 150 km from the storm center. In the inner-core region of TCs (radius <100 km), the rainfall frequency increases significantly around 3–9 h before the onset of RI and it continues to increase after RI begins (Fig. 3a). By the middle of RI events (i.e., >12 h after RI onset), the composite indicates that over 75% of the annulus between 30 and 70 km around the center is raining. However, while the rainfall frequency early in the RI event is increasing, the mean near-surface rain rate of that rainfall does not increase much until the middle of RI events (Fig. 3c). As mentioned above, total volumetric rain is determined by both the rainfall frequency and the near-surface rain rate, but the time evolution of total volumetric rain (not

TABLE 2. Number of selected PR overpasses before RI, during RI, and in the RI ending period. Also shown here is the number of selected PR overpasses in different future 24-h intensity change categories: RI, slowly intensifying (SI), neutral (*N*), and weakening (*W*).

Category		All	RI	SI	*N*	*W*
Before RI	36–48 h before	13	0	8	5	0
	24–36 h before	27	0	17	10	0
	18–24 h before	22	0	11	11	0
	12–18 h before	22	0	16	6	0
	6–12 h before	25	0	23	2	0
	0–6 h before	21	0	21	0	0
During RI	0–6 h after	19	19	0	0	0
	6–12 h after	23	23	0	0	0
	12–18 h after	22	22	0	0	0
	18–54 h after	31	31	0	0	0
RI ending	18–24 h before	23	0	23	0	0
	12–18 h before	28	0	28	0	0
	6–12 h before	24	0	12	11	1
	0–6 h before	12	0	3	6	3
All		312	95	162	51	4

shown) is more comparable to that of mean near-surface rain rate (Fig. 3c). There is almost no change of total volumetric rain within 9 h before RI onset and a substantial increase in total volumetric rain is only observed several hours after RI begins.

It should be noted that the results shown above are the mean values among the samples. To indicate the variability among all of the cases, the Hovmöller diagrams of the corresponding standard deviation are shown in the right column of Fig. 3. The large variability around 45 h prior to RI onset is a consequence of a small sample size (only a couple of cases), and thus is not a robust signal. However, as RI approaches, the sample size increases and the standard deviation decreases, indicating a more robust signal at those times. Overall, Fig. 3 suggests that the onset of RI is associated with a significant increase of rainfall frequency, while the delayed increase in rainfall intensity, as well as total volumetric rain, indicates that signal is more likely a result, or symptom, of RI, consistent with previous satellite-based studies (ZJ14; Tao and Jiang 2015).

b. *Shear-relative composites*

Composite images are applied in this part of study to further characterize the distributions of rainfall properties relative to vertical wind shear with respect to various RI event-based categories. The composites are generated by orientating the selected PR overpasses with the shear vector pointing upward along the $+y$ axis and the storm center in the middle. Overpasses in the Southern Hemisphere are flipped 180° before compositing with those of Northern Hemisphere, following Chen et al. (2006). The PR pixels, with their new shear-relative coordinates, are then averaged into $10 \times 10\,\text{km}^2$ grid cells, with the value of each grid cell representing the mean value of all PR pixels in that grid cell for each selected variable. Shear-relative images are described using a quadrant approach (Chen et al. 2006), with the upper-left, upper-right, lower-left, and lower-right quadrants referring to downshear left (DL), downshear right (DR), upshear left (UL), and upshear right (UR), respectively. The primary focus here is how the inner-core rainfall properties evolve relative to the direction of vertical wind shear from 12–24 h prior to the onset of RI to 12–24 h before RI ends.

1) RAINFALL FREQUENCY

The shear-relative composites of the percent occurrence of total rainfall in Fig. 4I shows a DL dominant distribution for all RI event-based categories, consistent with previous studies (e.g., Chen et al. 2006; Wingo and Cecil 2010; ZJ14). The rainfall frequency in the inner-core region of TCs keeps increasing until the beginning of RI ending period (Fig. 4Ie), and the increase is most significant within 12 h before the onset of RI, as

TABLE 3. Mean values of maximum sustained winds at current observational time (V_{max}), SST, vertical wind shear magnitude, TPW, storm motion, and the difference between the direction of vertical wind shear and storm motion vector for different RI event-based categories.

	Before RI			During RI		RI ending	
Category	24–48 h	12–24 h	0–12 h	RI initial	RI continuing	12 to ~24 h	0 to ~12 h
V_{max} (kt)	54.60	54.37	55.46	54.32	65.08[a]	59.71	70.73[a]
SST (°C)	28.65	28.46	28.61	28.49	28.69	28.41	28.02
Shear (m s^{-1})	5.82	6.68	6.14	6.57	4.78[b]	5.49	6.16
TPW (mm)	62.31	61.60	63.11	63.07	63.04	62.75	62.30
Motion (m s^{-1})	4.80	4.30	4.25	4.50	4.24	4.53	4.30
Shear − motion (°)	−60.42	−19.37	−57.35	−55.98	−75.38	−49.74	−74.64

[a] The statistical significance of the value from the value in the previous column at the 99.9% confidence level.
[b] The statistical significance of the value from the value in the previous column at the 99% confidence level.

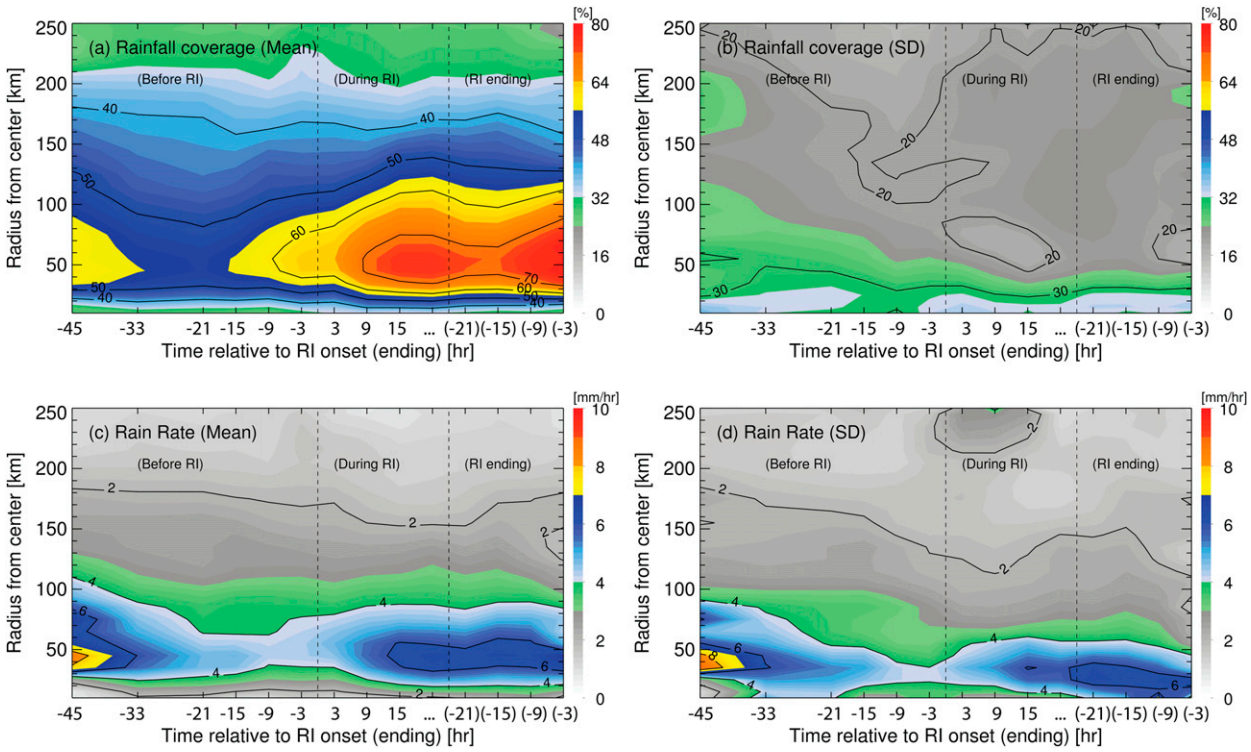

FIG. 3. Hovmöller diagrams of azimuthally averaged (a) rainfall coverage and (c) near-surface rain rate. (b),(d) The corresponding standard deviation, respectively. The averages are shown from the storm center out to 250 km. Dashed lines from left to right represent RI onset and 24 h before RI ends.

previously noted in Fig. 3a. The difference between −24 (Fig. 4Ia) and −12 h from RI onset (Fig. 4Ib) further indicates that the significant increase in the percent occurrence of total rainfall is mostly contributed by pixels in the UL quadrant, followed by pixels in the DR and UR quadrants (not shown). The percentage of pixels with nonzero near-surface rain rate continues to increase after RI begins. This increase concentrates in the upshear semicircle for storms within +12 h from RI onset (i.e., RI initial, Fig. 4Ic) and rotates cyclonically, concentrating to the right of the shear vector for storms that have been undergoing RI for over 12 h (i.e., RI continuing, Fig. 4Id). An increase of rainfall frequency, particularly upshear, and the subsequent greater azimuthal coverage of rainfall from 12 to 24 h before RI onset to the RI continuing stage, verify the importance of increasing the azimuthal rainfall symmetry around the TC center (Kieper and Jiang 2012; ZJ14; AZZ15). AZZ15 demonstrated a similar trend of increasing precipitation symmetry from before RI to after RI, indicating that the signal is robust, even with the more ambiguous RI case-based analysis method.

To examine how different precipitation types evolve, Figs. 4II and 4III shows the shear-relative composite image of the percent occurrence of stratiform and convective rainfall, respectively. Here, various types of precipitation are identified using the V7 of the TRMM PR 2A23 product. By applying the vertical profiling method (V method) and the horizontal pattern method (H method), the TRMM 2A23 classifies rain into three categories: stratiform, convective, and other (Awaka et al. 2009; Funk et al. 2013). Several updates have been added to the 2A23 algorithm for V7 to better distinguish the convective and stratiform precipitation. For example, the concepts of small rain cells and ''randomly'' appearing shallow nonisolated pixels are introduced in V7 to help further separating deep and shallow convective pixels [please refer to Funk et al. (2013) for more details]. Although the accuracy of pixel classification has improved in V7, uncertainties still remain for some of the identified rain types. Therefore, only the rain types that are denoted as ''stratiform certain'' (types 100 and 110) or ''convective certain'' (types 200, 210, and 220) in the V7 PR manual (TRMM Precipitation Radar Team 2011) are applied in this study, which represents the highest level of confidence. Although limiting the number of rain types to those of the highest confidence results in a lower fraction of rain echo classified as convective/stratiform compared

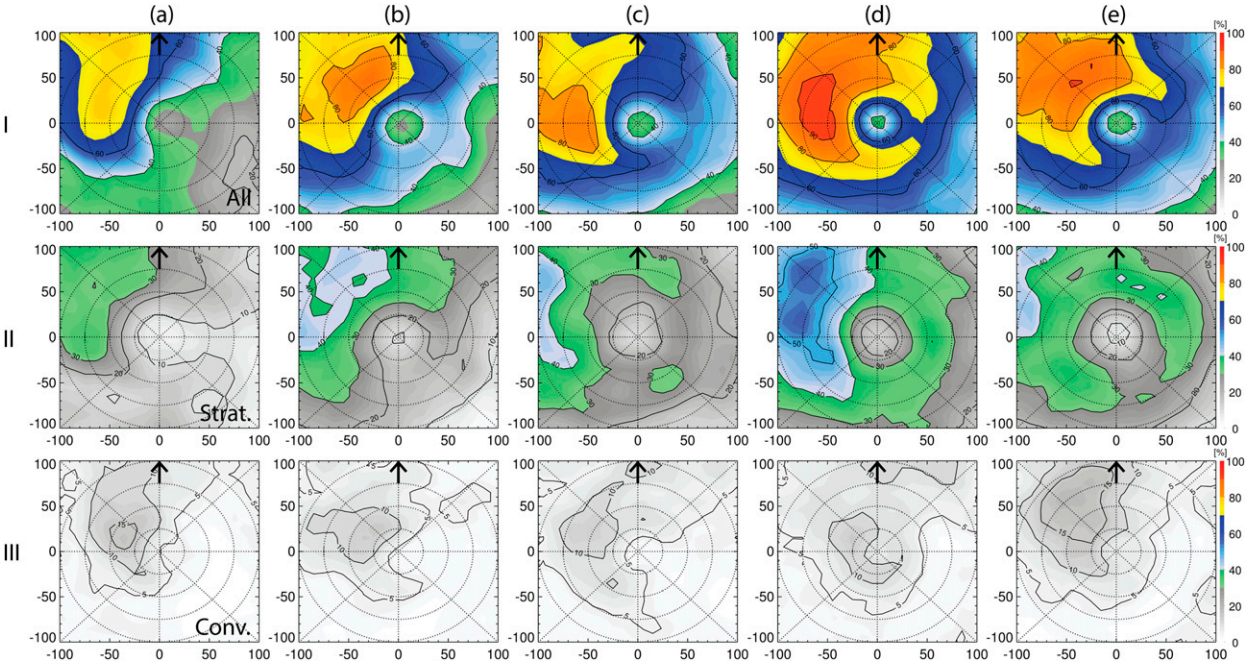

FIG. 4. Composite shear-relative distribution of the rainfall coverage from (I) all precipitation, (II) stratiform precipitation, and (III) convective precipitation. (a) 12–24 h before RI onset, (b) 0–12 h before RI onset, (c) RI initial, (d) RI continuing, and (e) 12–24 h before RI ends. Dotted range rings represent the 25-, 50-, 75-, and 100-km radii.

with the total, the distributions do not change noticeably.

As shown in Fig. 4II, about 55% of the total rainfall in the inner-core region of TCs is contributed by stratiform rain. This fraction is slightly lower than that in Schumacher and Houze (2003), which quantified that stratiform precipitation accounted for 73% of the raining area; this difference likely exists because of the consideration of only stratiform certain types in this study. More importantly, the significant increase in the rainfall frequency between the period of 12–24 and 0–12 h before RI onset is mainly due to a substantially increased frequency of stratiform rain (Figs. 4IIa and 4IIb). During the same period, however, the percent occurrence of convective rainfall decreases, especially left of the shear within 50 km from the storm center (Figs. 4IIIa and 4IIIb). The RI initial category shows a distinctly different distribution from those before RI onset. The convective rainfall frequency increases in the UL quadrant, and decreases DL, resulting in a more symmetric shear-relative distribution (Fig. 4IIIc). The overall appearance is more axisymmetric for the RI continuing category, with a ring of >5% convective rainfall frequency distributed completely around the center (Fig. 4IIId). The beginning of the RI ending period is characterized by a decrease in convective symmetry around the center, but an increase in convective rainfall frequency concentrated in the DL quadrant (Fig. 4IIIe). The convective maximum, however, is located farther from the storm center compared with the location observed prior to RI onset (Figs. 4IIIa,b).

2) MEAN RAIN RATE

Another aspect of the rainfall properties, in addition to the occurrence, that must be considered is the intensity of the rain, quantified here by the mean near-surface rain rate from 2A25. Before the onset of RI, a small area with mean rain rate exceeding 8 mm h^{-1} is observed in the DL quadrant (Figs. 5Ia,b). The intensity of the rain slightly decreases in the early stage of RI (Fig. 5Ic), as the heaviest precipitation is less than 8 mm h^{-1}. But the areal coverage of rain rate >6 mm h^{-1} increases, resulting in a more symmetric distribution for RI initial cases. Both the areal coverage of precipitation >6 mm h^{-1} and the intensity of the rain continue to increase in the middle of RI (Fig. 5Id). The intensity of the near-surface rain rate increases substantially from RI continuing to the beginning of RI ending period, as the heaviest precipitation rate is greater than 10 mm h^{-1} 12–24 h before RI ends (Fig. 5Ie).

As for different types of precipitation, the intensity of stratiform rain (Fig. 5II) is much weaker than that of convective rain (Fig. 5III) with most precipitation rates <4 mm h^{-1}. In addition, the rainfall intensity, as

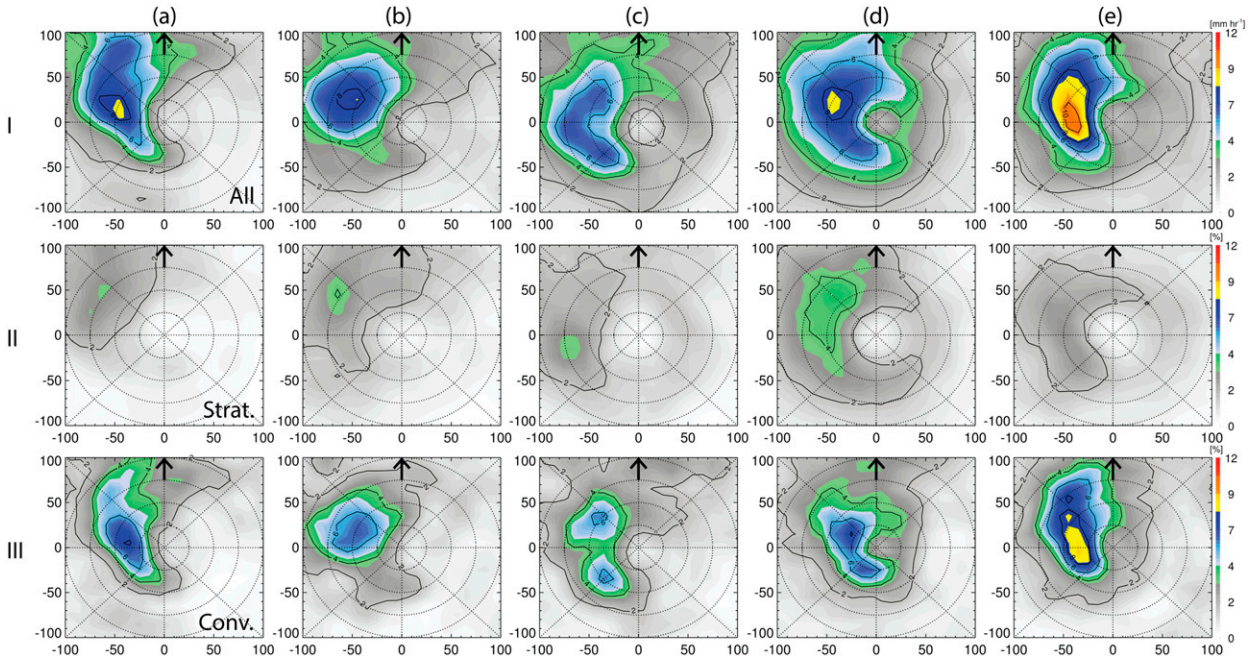

FIG. 5. As in Fig. 4, but for mean near-surface rain rate.

well as the areal coverage of rain rates >4 mm h^{-1}, does not increase much for stratiform rain until in the RI continuing period (Fig. 5IId). While the intensity of convective rain increases significantly left of the shear between 12 and 24 h before RI ends (Fig. 5IIIe), the intensity of stratiform rain decreases during the same period (Fig. 5IIe). For both stratiform and convective rain, the composite mean rain rate appears to rotate cyclonically from the DL to UL quadrant in the RI initial period, and becomes more symmetrically distributed (Figs. 5IIc and 5IIIc) compared with the DL-dominated pattern before RI onset (Figs. 5IIa,b and 5IIIa,b).

3) TOTAL VOLUMETRIC RAIN

Figure 6 shows the shear-relative composites of total volumetric rain for all precipitation (Fig. 6I), as well as separated into stratiform (Fig. 6II) and convective precipitation (Fig. 6III) components only. Generally, the distribution of total volumetric rain is similar to that of the mean near-surface rain rate (Fig. 5). In spite of a much lower rainfall frequency (Figs. 4II and 4III), convective rain quantitatively has a similar total volumetric rain as stratiform rain due to its intense rain rates. Additionally, the significant increase of total volumetric rain DL in the RI continuing stage has a predominant contribution from stratiform rain, while the period 12–24 h before RI ends is predominantly from convective rainfall. By comparing the total volumetric rain during RI period with before RI and RI ending periods, the results here further indicate that stratiform rain contributes more to total volumetric rain in storms during RI than those in non-RI periods (Fig. 6II); the opposite is true for convective rain (Fig. 6III), consistent with Tao and Jiang (2015).

4) AZIMUTHAL SYMMETRY OF THE RAINFALL DISTRIBUTIONS

To further quantify the azimuthal symmetry of the shear-relative distributions of rainfall coverage shown above (Fig. 4), an asymmetry index is generated for all types of rainfall, and stratiform and convective only with respect to various RI event-based categories and listed in Table 4. The methodology of the calculation of this asymmetry index is similar to that of AZZ15 (defined as "symmetry index" in their study). The asymmetry index of the rainfall coverage is created by first normalizing the quadrant mean of the rainfall coverage (averaged for all pixels within 100 km of the storm center) with the maximum value, and then by differencing the normalized mean value in each shear-relative quadrant. Only four out of six possible mean quadrant differences are applied here (UR − DR, UL − DL, UL − DR, and DL − UR), following AZZ15, as the absolute value of these four quadrant differences contribute most to the distinctions among various RI event-based categories. Therefore, the lower the value of the asymmetry index, the greater the degree of the azimuthal symmetry.

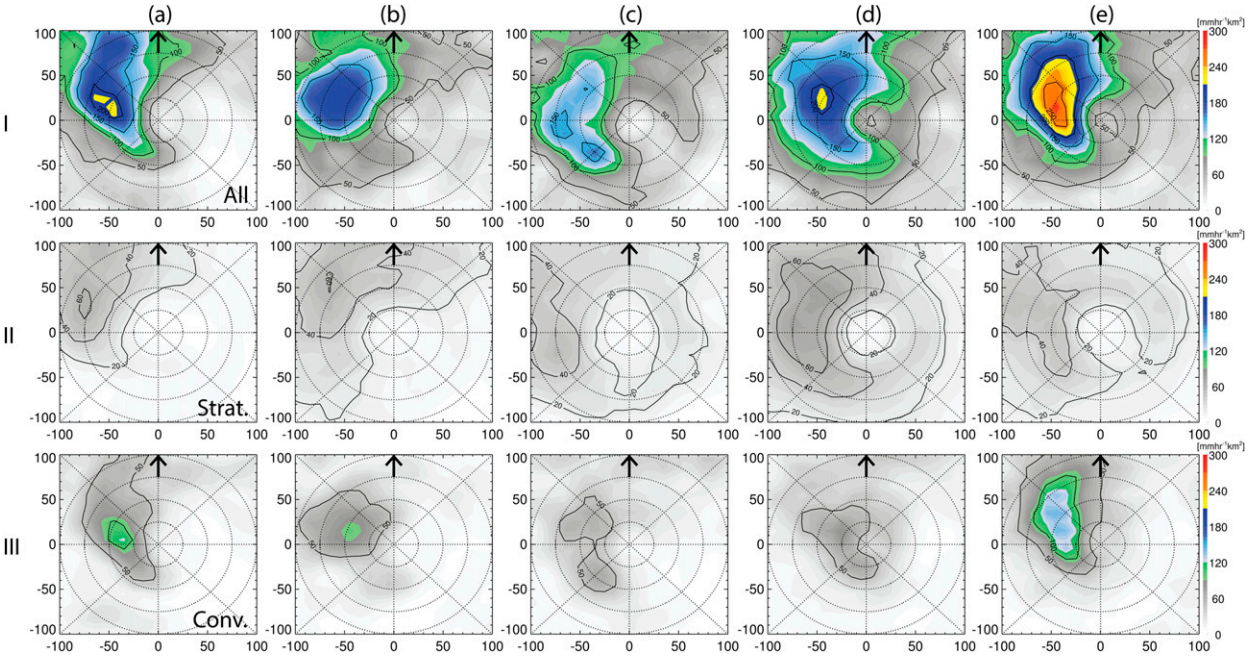

FIG. 6. As in Fig. 4, but for total volumetric rain.

For all types of precipitation, the asymmetry index of the rainfall coverage decreases as RI onset nears and continues to decrease during the RI continuing stage, while an increase of the asymmetry index is observed during the RI ending period (Table 4). This is consistent with AZZ15's study, which showed that RI storms present much greater azimuthal precipitation symmetry compared with SI storms. Overall, this time evolution suggests that a quantitative estimate of the degree of precipitation symmetry (e.g., asymmetry index) has applicability for forecasting RI events.

As for the individual precipitation types, Table 4 shows that the symmetry of the rainfall coverage increases (lower values of the asymmetry index) from 12 to 24 h before RI onset to RI initial for both stratiform and convective rainfall, and the rate of symmetry increase is much higher for stratiform $[0.8\ (24\,\mathrm{h})^{-1}]$ compared with convective $[0.3\ (24\,\mathrm{h})^{-1}]$. In contrast, the convective rainfall symmetry increases slightly from the RI initial to RI continuing stage, while the stratiform rainfall symmetry decreases slightly during the same period.

4. Comparison with null cases

a. Dataset of SI storms as null cases

Discussions above focus on various stages of RI events and indicate that the onset of RI follows a significant increase in the areal coverage of stratiform precipitation around the TC center. However, to fully examine the relative importance of different types of precipitation to RI requires a comparison with the null cases (i.e., storms that do not undergo RI during their life cycle). The most important question to be addressed here is whether RI is predictable such that the difference in the rainfall properties in the period just prior to RI onset could explain why some storms experience RI while some others do not. As shown in Table 2, most storms experience SI before undergoing RI. For this reason, two groups of SI cases are considered in this section: one for RI storms (i.e., SI cases that are 0–12 h before RI onset), the other for non-RI storms (i.e., SI cases that never experience an RI event). The definition and sample size for each SI group are summarized in Table 5.

TABLE 4. Asymmetry index for the rainfall coverage with respect to various RI event-based categories. Also shown here is the asymmetry index for the rainfall coverage of all types of rain, stratiform, and convective rainfall only, respectively.

	Rain type	12–24 h before RI onset	0–12 h before RI onset	RI initial	RI continuing	0–12 h before RI ends
Rainfall coverage	All	1.22	0.99	0.68	0.57	0.76
	Stratiform	1.23	1.12	0.42	0.64	0.35
	Convective	1.60	1.38	1.30	1.14	1.52

TABLE 5. Definition and number of PR overpasses for two groups of SI cases: one group from storms that undergo RI and the other from storms that never rapidly intensify during their life cycle; V_{max}, V_{max+6}, V_{max+24}, and V_{max+30} represent the maximum sustained wind at current time, and 6, 24, and 30 h in future, respectively.

SI cases	Definition	No. of overpasses
RI storms	0–12 h before RI onset and $10 \le V_{max+24} - V_{max} < 30$ kt	44
Non-RI storms	$10 \le V_{max+24} - V_{max} < 30$ kt and $10 \le V_{max+30} - V_{max+6} < 30$ kt	96

Before a detailed examination of the differences in the rainfall properties between RI and non-RI storms, the environmental conditions, as well as the storm properties are first analyzed (Table 6). The results in Table 6 indicate that the environments between SI cases that undergo RI within +12 h versus those that do not are not significantly different, with the exception of the fact that storms that undergo RI are somewhat more intense (higher maximum sustained winds) just prior to the onset of RI (0–12 h before). Considering the lack of differences in the environments (i.e., SST, shear, TPW, and motion), this result strongly suggests that the precipitation properties differentiate those storms that eventually undergo RI versus those that only undergo SI.

b. *Shear-relative composites*

The shear-relative composite image of the rainfall frequency shows the expected DL dominant distribution for both of the defined SI groups (Figs. 7Ia,b). But RI storms (Fig. 7Ia) have much higher occurrence and areal coverage of rainfall than those that do not undergo RI during their lifetime (Fig. 7Ib), with a ring of 40% occurrence of rainfall distributed completely around the TC center. This is more clearly shown by the difference between the two groups (Fig. 7Ic). The positive value is observed nearly everywhere within the innermost 100-km area, with the largest difference located in the UL quadrant. Stratiform rain is the largest contributor to this positive difference (Fig. 7IIc), while the difference in all shear-relative quadrants between RI and non-RI storms for convective occurrence is noticeably smaller (Fig. 7IIIc).

Similarly, Fig. 8 shows the shear-relative composites of total volumetric rain for RI and non-RI storms. Consistent with the rainfall frequency, RI storms (Fig. 8Ia) present much greater total volumetric rain than those that never rapidly intensify during their life cycle (Fig. 8Ib). But the peak of the positive differences between these two SI groups concentrate in the DL quadrant (Fig. 8Ic), which is different from the UL peak of the positive differences in rainfall frequency (Fig. 7Ic). Additionally, in contrast to the rainfall coverage, which shows that stratiform rain contributes a greater fraction of the differences (Fig. 7II), the convective rainfall accounts for the majority of the positive differences between RI and non-RI storms in total volumetric rain (Fig. 8IIIc). Results indicate that differences in total volumetric rain predominantly come from the rain rate, which has a very similar distribution to total volumetric rain for both RI and non-RI storms (not shown).

5. Discussion and conclusions

Based on 16 years of observations from TRMM PR, the evolution of rainfall properties in the inner-core region (radius <100 km) of TCs is examined in terms of RI events. Consistent with previous satellite-based studies (e.g., Jiang and Ramirez 2013; ZJ14, AZZ15), storms during RI (both RI initial and RI continuing) feature greater percent occurrence of total rainfall and a more symmetric shear-relative azimuthal distribution than those before RI onset and in the RI ending period.

By comparing the distributions before and after RI onset, this study further indicates that the onset of RI is closely associated with an increased rainfall frequency (defined in this study as the percent occurrence of PR 2A25 near-surface rain rate $>0\,mm\,h^{-1}$) and areal coverage of rainfall around the storm center. A significant increase in the rainfall frequency is particularly noted around 3–9 h prior to RI onset, which in turn could be used as a potential predictor in forecasts of the onset of RI (Fig. 3a). The shear-relative composites show that

TABLE 6. Mean values of maximum sustained winds at current observational time (V_{max}), SST, vertical wind shear magnitude, TPW, storm motion, and the difference between the direction of vertical wind shear and storm motion vector for RI and non-RI storms.

SI cases	V_{max} (kt)	SST (°C)	Shear ($m\,s^{-1}$)	TPW (mm)	Motion ($m\,s^{-1}$)	Shear − motion (°)
RI storms	55.3[a]	28.6	6.3	63.2	4.3	−64.8
Non-RI storms	48.8	28.4	6.4	63.0	4.3	−47.6

[a] The statistical significance of the value from the value in the previous column at the 95% confidence level.

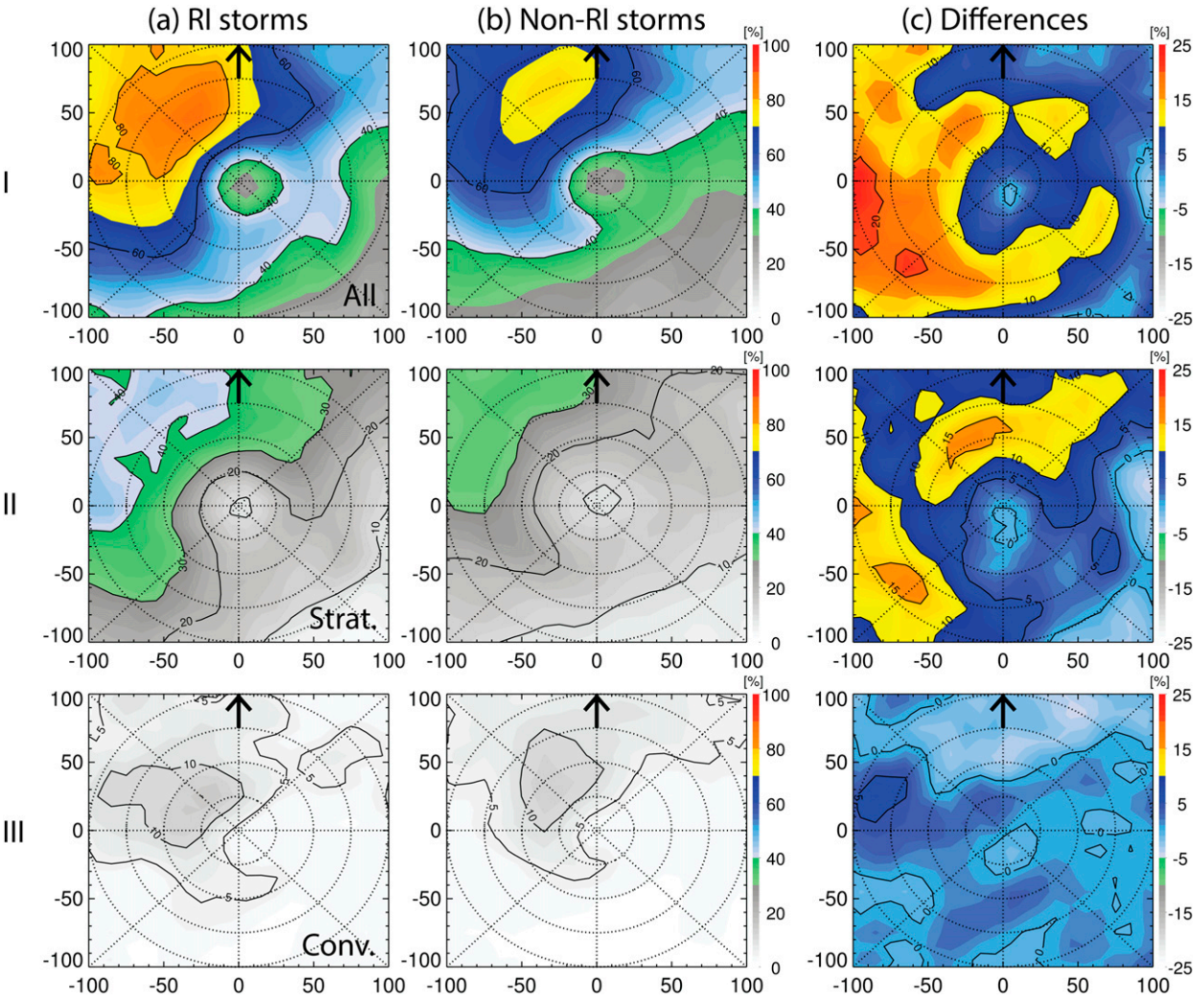

FIG. 7. Composite shear-relative distributions of the rainfall coverage from (I) all precipitation, (II) stratiform precipitation, and (III) convective precipitation. (a) SI cases from RI storms (i.e., 0–12 h before RI onset), (b) SI cases from non-RI storms, and (c) difference between SI cases from RI and from non-RI storms. Dotted range rings represent the 25-, 50-, 75-, and 100-km radii.

the increase in the rainfall frequency is first observed in the UL quadrant 0–12 h before RI onset and then rotates cyclonically as RI continues, concentrating in the UR quadrant for RI initial storms and right of the shear vector during the RI continuing period (Fig. 4). Both rainfall intensity (defined in this study as the mean near-surface rain rate) and total volumetric rain do not increase much until several hours after RI onset (Figs. 3, 5, and 6), suggesting that the much higher rainfall intensity and total volumetric rain noted for RI storms are more likely a response, rather than a trigger, of RI. The beginning of the RI ending period (a 24-h period before RI ends) follows a significant decrease in the areal coverage of total rainfall right of the shear vector. As such, the RI ending period exhibits a more asymmetric distribution compared with the RI continuing stage, as evidenced by a substantial increase in the rainfall intensity and total volumetric rain observed DL during this period and decrease in other shear-relative quadrants.

The time evolution of the asymmetry index, which is a quantitative measure of the degree of symmetry of the distributions, indicates an increase in azimuthal precipitation symmetry (decrease in asymmetry index) from 12 to 24 h before RI onset to RI continuing, and a decrease in symmetry (increase in asymmetry index) from RI continuing to 12–24 h before RI ends (Table 4). This composite time evolution could be potentially useful toward improving the RI forecasts of individual storms.

The relative importance of stratiform and convective rainfall, differentiated by the ''certain'' types in the TRMM 2A23 algorithm, to the total rainfall distribution

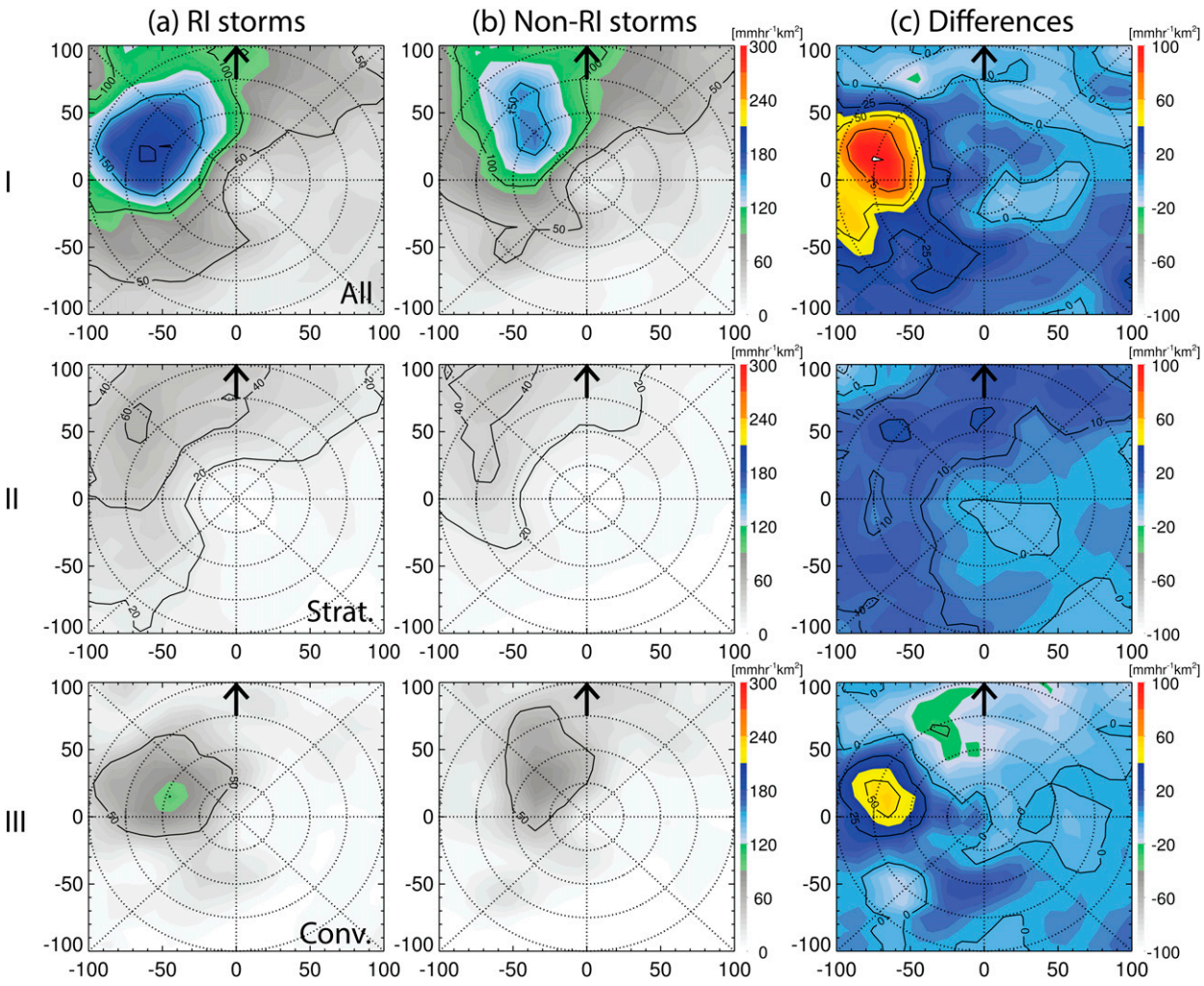

FIG. 8. As in Fig. 7, but for total volumetric rain.

in RI events is also examined. The results strongly suggest that stratiform rainfall predominantly contributes over convection toward the significantly increased rainfall coverage around 3–9 h prior to RI onset (Fig. 4IIb). A comparison with non-RI storms (those SI storms that do not experience an RI event) further confirms the importance of stratiform precipitation toward increasing the occurrence and areal coverage of rainfall around the storm center that characterizes RI events. Statistically, storms that never rapidly intensify during their life cycle have much lower rainfall coverage of stratiform rain, particularly upshear, within the inner-core region of TCs compared with RI storms (Fig. 7). Note that due to the sensitivity of the TRMM PR (i.e., limited to reflectivity >17 dBZ), some weak precipitation, especially in the upshear quadrants are not detected, likely resulting in an underestimation of the percentages of stratiform precipitation in this study.

The increased azimuthal coverage of stratiform rain in RI events likely coincides with moistening/humidification of the inner core, especially in the upshear quadrants. Zawislak et al. (2016) demonstrate an example of this relationship in Hurricane Edouard (2014) using a synthesis of rainfall (derived from infrared and passive microwave sensors) and thermodynamic (from high-altitude dropsonde observations from the NASA Global Hawk) properties. Although Edouard does not qualify as a RI storm in this study (it experienced a brief RI event of 9 h, which is well under our 24-h requirement), Zawislak et al. (2016) find that an increase in precipitation symmetry during the intensification of Edouard coincides with a systematic increase in mid- to upper-tropospheric humidity in the upshear quadrants. Our study could help explain further what type of precipitation is responsible for the moistening/humidification. It is hypothesized here that the increased

occurrence and areal coverage of stratiform rain 0–12 h before RI onset can contribute toward removing unfavorable and relatively dry layers (cf. downshear) in the upshear quadrants, which leads to a more symmetric rainfall and latent heating distribution after RI begins. The symmetric heating mechanism has been long known as the preferred mechanism for TC intensification (Ooyama 1969; Nolan et al. 2007). In this pathway, the stratiform rain humidifies the troposphere from the top down as the rain rate increases. An alternative pathway is that shallow to moderately deep convection humidifies from the bottom up, but given the lower occurrence of convection compared to stratiform, this pathway would be less dominant. Considering the uncertainties in 2A23 related to the convective rain identification, other datasets are required to further evaluate which pathway is responsible for moistening/humidification.

The contribution by convective precipitation in RI storms is mostly attributed to an increasing rainfall intensity (rain rate) and total volumetric rain within the inner-core region. Storms in the early stage of RI are differentiated from those 0–12 h before RI onset in that there is significantly larger convective occurrence, higher convective rainfall intensity, and greater convective volumetric rain UL (Figs. 4III, 5III, and 6III). This is generally consistent with previous studies (e.g., Stevenson et al. 2014; ZJ14; Rogers et al. 2015, 2016; Chen and Gopalakrishnan 2015; AZZ15), which indicated the presence of deep convection in the UL quadrant as being a key feature for intensifying TCs. The relatively greater convective precipitation UL may possible be due to favorable conditioning (humidity/moisture increase) from the increased stratiform rain occurrence in the upshear quadrants ~12 h earlier.

The results here document the evolution of different types of precipitation for RI storms. One of the most significant findings is the importance of an increased azimuthal coverage of stratiform rain several hours before RI onset. The increase in the stratiform occurrence is observed in all shear-relative quadrants, especially UL. The relatively greater areal coverage of stratiform rain 0–12 h before RI onset could result from the transport of hydrometers from the DL quadrant, owing to the increasing swirling winds around the TC center. Future work using numerical models and trajectory calculations are needed to better classify the mechanisms that lead to the increased occurrence of precipitation in the upshear quadrants. Besides the inner-core distributions of rainfall and convection, changes in the wind and moisture fields, and the vortex structure prior to and near RI onset are important as well. Studies based on finer temporal and horizontal resolutions are desired to better understand the physical processes triggering the onset of RI.

Acknowledgments. The authors thank Dr. Frank Marks and Mr. Bradley Klotz for their helpful insights on this work. Thanks are also due to Mr. Joseph Zagrodnik, Dr. Tie Yuan, and Prof. Chuntao Liu for TRMM data processing assistance. The constructive comments from three anonymous reviewers are appreciated and contribute greatly in improving the manuscript. This research was supported by NASA Earth and Space Science Fellowship (NESSF) Award NNX11AL66H and Florida International University (FIU) Dissertation Year Fellowship (DYF). Additional support was provided by NASA New Investigator Program (NIP) Award NNX10AG55G, NASA Hurricane Science Research Program (HSRP) Grant NNX10AG34G under the direction of Drs. Ramesh Kakar and Ming-Ying Wei, and NOAA Joint Hurricane Testbed (JHT) Grants NA11OAR4310193, NA13OAR4590191, and NA15OAR4590199 under the direction of Dr. Chris Landsea.

REFERENCES

Alvey, G., III, J. Zawislak, and E. J. Zipser, 2015: Precipitation properties observed during tropical cyclone intensity change. *Mon. Wea. Rev.*, **143**, 4476–4492, doi:10.1175/MWR-D-15-0065.1.

Awaka, J., T. Iguchi, and K. Okamoto, 2009: TRMM PR standard algorithm 2A23 and its performance on bright band detection. *J. Meteor. Soc. Japan*, **87A**, 31–52, doi:10.2151/jmsj.87A.31.

Chen, H., and S. G. Gopalakrishnan, 2015: A study on the asymmetric rapid intensification of Hurricane Earl (2010) using the HWRF system. *J. Atmos. Sci.*, **72**, 531–550, doi:10.1175/JAS-D-14-0097.1.

Chen, S. S., J. A. Knaff, and F. D. Marks, 2006: Effects of vertical wind shear and storm motion on tropical cyclone rainfall asymmetries deduced from TRMM. *Mon. Wea. Rev.*, **134**, 3190–3208, doi:10.1175/MWR3245.1.

DeMaria, M., C. R. Sampson, J. A. Knaff, and K. D. Musgrave, 2014: Is tropical cyclone intensity guidance improving? *Bull. Amer. Meteor. Soc.*, **95**, 387–398, doi:10.1175/BAMS-D-12-00240.1.

Fritz, C., Z. Wang, S. W. Nesbitt, and T. J. Dunkerton, 2016: Vertical structure and contribution of different types of precipitation during Atlantic tropical cyclone formation as revealed by TRMM PR. *Geophys. Res. Lett.*, **43**, 894–901, doi:10.1002/2015GL067122.

Funk, A., C. Schumacher, and J. Awaka, 2013: Analysis of rain classifications over the tropics by version 7 of the TRMM PR 2A23 algorithm. *J. Meteor. Soc. Japan*, **91**, 257–272, doi:10.2151/jmsj.2013-302.

Guimond, S. R., G. M. Heymsfield, and F. J. Turk, 2010: Multiscale observations of Hurricane Dennis (2005): The effects of hot towers on rapid intensification. *J. Atmos. Sci.*, **67**, 633–654, doi:10.1175/2009JAS3119.1.

Harnos, D. S., and S. W. Nesbitt, 2016: Varied pathways for simulated tropical cyclone rapid intensification. Part II: Vertical motion and cloud populations. *Quart. J. Roy. Meteor. Soc.*, **142**, 1832–1846, doi:10.1002/qj.2778.

Hence, D. A., and R. A. Houze Jr., 2011: Vertical structure of hurricane eyewalls as seen by the TRMM Precipitation Radar. *J. Atmos. Sci.*, **68**, 1637–1652, doi:10.1175/2011JAS3578.1.

Hendricks, E. A., M. T. Montgomery, and C. A. Davis, 2004: The role of "vortical" hot towers in the formation of Tropical Cyclone Diana (1984). *J. Atmos. Sci.*, **61**, 1209–1232, doi:10.1175/1520-0469(2004)061<1209:TROVHT>2.0.CO;2.

——, M. S. Peng, B. Fu, and T. Li, 2010: Quantifying environmental control on tropical cyclone intensity change. *Mon. Wea. Rev.*, **138**, 3243–3271, doi:10.1175/2010MWR3185.1.

Houze, R. A., Jr., 2010: Clouds in tropical cyclones. *Mon. Wea. Rev.*, **138**, 293–344, doi:10.1175/2009MWR2989.1.

Iguchi, T., T. Kozu, J. Kwiatkwoski, R. Meneghini, J. Awaka, and K. Okamoto, 2009: Uncertainties in the rain profiling algorithm for the TRMM precipitation radar. *J. Meteor. Soc. Japan*, **87A**, 1–30, doi:10.2151/jmsj.87A.1.

Jiang, H., 2012: The relationship between tropical cyclone intensity change and the strength of inner-core convection. *Mon. Wea. Rev.*, **140**, 1164–1176, doi:10.1175/MWR-D-11-00134.1.

——, and E. M. Ramirez, 2013: Necessary conditions for tropical cyclone rapid intensification as derived from 11 years of TRMM data. *J. Climate*, **26**, 6459–6470, doi:10.1175/JCLI-D-12-00432.1.

——, C. Liu, and E. J. Zipser, 2011: A TRMM-based tropical cyclone cloud and precipitation feature database. *J. Appl. Meteor. Climatol.*, **50**, 1255–1274, doi:10.1175/2011JAMC2662.1.

Kaplan, J., and M. DeMaria, 2003: Large-scale characteristics of rapidly intensifying tropical cyclones in the North Atlantic basin. *Wea. Forecasting*, **18**, 1093–1108, doi:10.1175/1520-0434(2003)018<1093:LCORIT>2.0.CO;2.

——, ——, and J. A. Knaff, 2010: A revised tropical cyclone rapid intensification index for the Atlantic and eastern North Pacific basins. *Wea. Forecasting*, **25**, 220–241, doi:10.1175/2009WAF2222280.1.

——, and Coauthors, 2015: Evaluating environmental impacts on tropical cyclone rapid intensification predictability utilizing statistical models. *Wea. Forecasting*, **30**, 1374–1396, doi:10.1175/WAF-D-15-0032.1.

Kelley, O. A., J. Stout, and J. B. Halverson, 2004: Tall precipitation cells in tropical cyclone eyewalls are associated with tropical cyclone intensification. *Geophys. Res. Lett.*, **31**, L24112, doi:10.1029/2004GL021616.

Kieper, M. E., and H. Jiang, 2012: Predicting tropical cyclone rapid intensification using the 37 GHz ring pattern identified from passive microwave measurements. *Geophys. Res. Lett.*, **39**, L13804, doi:10.1029/2012GL052115.

Nolan, D. S., and L. D. Grasso, 2003: Nonhydrostatic, three-dimensional perturbations to balanced, hurricane-like vortices. Part II: Symmetric response and nonlinear simulations. *J. Atmos. Sci.*, **60**, 2717–2745, doi:10.1175/1520-0469(2003)060<2717:NTPTBH>2.0.CO;2.

——, Y. Moon, and D. P. Stern, 2007: Tropical cyclone intensification from asymmetric convection: Energetics and efficiency. *J. Atmos. Sci.*, **64**, 3377–3405, doi:10.1175/JAS3988.1.

Ooyama, K., 1969: Numerical simulation of the life cycle of tropical cyclones. *J. Atmos. Sci.*, **26**, 3–40, doi:10.1175/1520-0469(1969)026<0003:NSOTLC>2.0.CO;2.

Reasor, P. D., M. D. Eastin, and J. F. Gamache, 2009: Rapidly intensifying Hurricane Guillermo (1997). Part I: Low-wavenumber structure and evolution. *Mon. Wea. Rev.*, **137**, 603–631, doi:10.1175/2008MWR2487.1.

Reynolds, R. W., T. M. Smith, C. Liu, D. B. Chelton, K. S. Casey, and M. G. Schlax, 2007: Daily high-resolution-blended analyses for sea surface temperature. *J. Climate*, **20**, 5473–5496, doi:10.1175/2007JCLI1824.1.

Rogers, R. F., P. D. Reasor, and S. Lorsolo, 2013: Airborne Doppler observations of the inner-core structural differences between intensifying and steady-state tropical cyclones. *Mon. Wea. Rev.*, **141**, 2970–2991, doi:10.1175/MWR-D-12-00357.1.

——, ——, and J. A. Zhang, 2015: Multiscale structure and evolution of Hurricane Earl (2010) during rapid intensification. *Mon. Wea. Rev.*, **143**, 536–562, doi:10.1175/MWR-D-14-00175.1.

——, J. A. Zhang, J. Zawislak, H. Jiang, G. R. Alvey, E. J. Zipser, and S. N. Stevenson, 2016: Observations of the structure and evolution of Hurricane Edouard (2014) during intensity change. Part II: Kinematic structure and the distribution of deep convection. *Mon. Wea. Rev.*, **144**, 3355–3376, doi:10.1175/MWR-D-16-0017.1.

Schumacher, C., and R. A. Houze Jr., 2003: Stratiform rain in the tropics as seen by the TRMM Precipitation Radar. *J. Climate*, **16**, 1739–1756, doi:10.1175/1520-0442(2003)016<1739:SRITTA>2.0.CO;2.

Shapiro, L. J., and H. E. Willoughby, 1982: The response of balanced hurricanes to local sources of heat and momentum. *J. Atmos. Sci.*, **39**, 378–394, doi:10.1175/1520-0469(1982)039<0378:TROBHT>2.0.CO;2.

Simmons, A., S. Uppala, D. Dee, and S. Kobayashi, 2007: ERA-Interim: New ECMWF reanalysis products from 1989 onwards. *ECMWF Newsletter,* No. 110, ECMWF, Reading, United Kingdom, 26–35.

Smith, R. K., 1981: The cyclostrophic adjustment of vortices with application to tropical cyclone modification. *J. Atmos. Sci.*, **38**, 2021–2030, doi:10.1175/1520-0469(1981)038<2021:TCAOVW>2.0.CO;2.

Stevenson, S. N., K. L. Corbosiero, and J. Molinari, 2014: The convective evolution and rapid intensification of Hurricane Earl (2010). *Mon. Wea. Rev.*, **142**, 4364–4380, doi:10.1175/MWR-D-14-00078.1.

Susca-Lopata, G., J. Zawislak, E. J. Zipser, and R. F. Rogers, 2015: The role of observed environmental conditions and precipitation evolution in the rapid intensification of Hurricane Earl (2010). *Mon. Wea. Rev.*, **143**, 2207–2223, doi:10.1175/MWR-D-14-00283.1.

Tao, C., and H. Jiang, 2015: Distributions of shallow to very deep precipitation-convection in rapidly intensifying tropical cyclones. *J. Climate*, **28**, 8791–8824, doi:10.1175/JCLI-D-14-00448.1.

TRMM Precipitation Radar Team, 2011: Tropical Rainfall Measuring Mission (TRMM) precipitation radar algorithm: Instruction manual for version 7. JAXA-NASA, 170 pp. [Available online at http://www.eorc.jaxa.jp/TRMM/documents/PR_algorithm_product_information/pr_manual/PR_Instruction_Manual_V7_L1.pdf.]

Wang, Y., and C.-C. Wu, 2004: Current understanding of tropical cyclone structure and intensity changes—A review. *Meteor. Atmos. Phys.*, **87**, 257–278, doi:10.1007/s00703-003-0055-6.

Willoughby, H. E., J. A. Clos, and M. G. Shoreibah, 1982: Concentric eye walls, secondary wind maxima, and the development of the hurricane vortex. *J. Atmos. Sci.*, **39**, 395–411, doi:10.1175/1520-0469(1982)039<0395:CEWSWM>2.0.CO;2.

Wingo, M. T., and D. J. Cecil, 2010: Effects of vertical wind shear on tropical cyclone precipitation. *Mon. Wea. Rev.*, **138**, 645–662, doi:10.1175/2009MWR2921.1.

Zagrodnik, J. P., and H. Jiang, 2014: Rainfall, convection, and latent heating distributions in rapidly intensifying tropical cyclones. *J. Atmos. Sci.*, **71**, 2789–2809, doi:10.1175/JAS-D-13-0314.1.

Zawislak, J., H. Jiang, G. R. Alvey, E. J. Zipser, R. F. Rogers, J. A. Zhang, and S. N. Stevenson, 2016: Observations of the structure and evolution of Hurricane Edouard (2014) during intensity change. Part I: Relationship between the thermodynamic structure and precipitation. *Mon. Wea. Rev.*, **144**, 3333–3354, doi:10.1175/MWR-D-16-0018.1.